**Grubraw, a chemogenetic generator of mitochondrial pyruvate, reveals new mechanisms of mitochondrial metabolic control that underlie the Warburg effect**

Ekaterina S. Potekhina[1,2]*, Dina Y. Bass[1,2]*, Alexander V. Ivanenko[1,2], Alexander A. Moshchenko[3], Dmitri A. Korzhenevskiy[3], Anastasia E. Karnaeva[4], Natalia F. Zakirova[5], Alexander V. Ivanov[5], Liubov E. Shimolina[6], Marina V. Shirmanova[6], Olga V. Lyang[3], Olga I. Patsap[3], Ivan Bogeski[7], Alexey M. Nesterenko[3], Vsevolod V. Belousov[1,2,3,7]

[1]Shemyakin-Ovchinnikov Institute of Bioorganic Chemistry, Moscow, Russia
[2]Center for Precision Genome Editing and Genetic Technologies for Biomedicine, Pirogov Russian National Research Medical University, Moscow, Russia
[3]Federal Center of Brain Research and Neurotechnologies, Federal Medical Biological Agency, Moscow, Russia
[4]Frumkin Institute Of Physical Chemistry And Electrochemistry, Russian Academy Of Sciences, Moscow, Russia
[5]Center for Precision Genome Editing and Genetic Technologies for Biomedicine, Engelhardt Institute of Molecular Biology, Russian Academy of Sciences, Moscow, Russia
[6]Institute of Experimental Oncology and Biomedical Technologies, Privolzhsky Research Medical University, Nizhny Novgorod, Russia
[7]Molecular Physiology Division, Institute of Cardiovascular Physiology, University Medical Center, Georg-August University Göttingen, Germany.

*These authors contributed equally to this work.

**Abstract**
Upregulation of glycolysis and downregulation of mitochondrial oxidative phosphorylation, termed as the Warburg effect, are characteristic of tumor cells[1,2]. Restriction of pyruvate flux into the mitochondrial matrix is one of the major mechanisms underlying this phenomenon[3]. Warburg-type metabolism is beneficial for rapidly proliferating cells, however its function remains unclear. Moreover, it is unknown what the metabolic consequences of activation of mitochondrial respiration in Warburg-type cancer cells are. Here we created a chemogenetic instrument, Grubraw, that generates pyruvate directly in the mitochondrial matrix bypassing restricted pyruvate influx. In cancer cells, Grubraw-driven pyruvate synthesis in the matrix increased mitochondrial membrane potential, oxygen consumption rate, and the amounts of TCA cycle intermediates. In a mouse model of human melanoma xenografts, chemogenetic activation of mitochondria caused a decrease in tumor growth rate. Surprisingly, cancer cells actively exported pyruvate generated by Grubraw in the mitochondria into the extracellular medium. Our results demonstrate that cells with Warburg-type metabolism use a previously unknown mechanism of carbon flux control to dispose of excessive mitochondrial pyruvate.

**Main**
Pyruvate is one of the key molecules critical to eukaryotic metabolism as the endpoint of glycolysis and an important branching point between lactic fermentation and oxidative phosphorylation (OXPHOS). In cancer cells, pyruvate is one of the keystone molecules for metabolic reprogramming, termed the Warburg effect. Current understanding describes the Warburg phenotype as metabolic reprogramming associated with upregulation of glycolysis and downregulation of OXPHOS[1,2]. Carcinogenesis and the Warburg effect are frequently accompanied by decreased pyruvate entry into mitochondria via mitochondrial pyruvate carrier

(MPC)[3,4]. Moreover, pyruvate metabolism plays a significant role in tumor angiogenesis[5], epithelial-mesenchymal transition (EMT),the development of chemoresistance in cancer cells[6], and HIF-1α degradation inhibition under aerobic conditions[7]. Why cancer cells restrict mitochondrial function, and what the metabolic and phenotypic consequences are if mitochondria in cancer cells are forced to metabolize pyruvate and respire intensively remains unknown.

In order to force mitochondria in cancer cells to metabolize pyruvate and respire more intensively we have developed a chemogenetic molecular tool based on *Pseudomonas aeruginosa* FAD-dependent D-amino acid dehydrogenase DadA that allows bypass of the pyruvate transport block and activation of mitochondrial respiration by generating pyruvate from D-alanine directly in the mitochondria of eukaryotic cells and donating electrons downstream of Complex I. DadA-dependent oxidative deamination of D-alanine leads to production of pyruvate and ammonia, involving an unknown electron acceptor for $FADH_2$ (Fig. 1a)[8]. Since D-alanine is absent in most mammalian tissues, except the brain and pancreas[9,10], DadA activity in the cells can be regulated by external administration of D-alanine.

The fusion proteins mRuby-DadA and EGFP-DadA, retaining near-native enzymatic activity, were created to enable DadA tracking in live cells (Extended Data Fig. 1a). To control the unspecific effects of heterologous protein expression, an inactive mutant was created by changing the conservative Tyr17 and Tyr18 residues in the predicted FAD-binding domain to Ala residues (Extended Data Fig. 1b, 1a).

The fusion proteins were targeted to the mitochondrial matrix, and mitochondrial localization was confirmed by imaging with the mitochondria-specific dyes TMRM or MitoTracker Green (Fig. 1b, S1c, S1d). Mito-mRuby-DadA matrix localization in HeLa Kyoto was confirmed by coexpressing with Micos60-HyPer7 protein localized in the mitochondrial intermembrane space (Fig. 1c). The fluorescence intensity profile along the mitochondrion cross-section showed that the mRuby fluorescence peak was located between two HyPer7 fluorescence peaks, confirming that all observed DadA was localized in the mitochondrial matrix (Fig. 1d). Since the purpose of our study was to reverse the Warburg effect, we named the mitochondrial DadA version fused to the fluorescent protein **Grubraw** (reversed Warburg).

To directly monitor pyruvate dynamics in the cytosol and mitochondrial matrix of HeLa cells expressing Grubraw, we used Pyrates[11], a genetically encoded fluorescent sensor for pyruvate. To prove that Grubraw generates pyruvate in the matrix when supplied with the substrate, we removed glucose from the cell culture medium, and inhibited pyruvate entrance to the TCA cycle using the inhibitor of pyruvate dehydrogenase CPI-613. Upon D-Ala addition, we observed a significant increase in matrix pyruvate concentration (Fig. 1e). Grubraw activity did not affect the concentration of pyruvate in the cytosol (Fig. 1f) suggesting that HeLa cells maintain a steady pyruvate concentration in this compartment.

We were also interested in whether loading the mitochondrial matrix with pyruvate could enhance electron transport chain (ETC) function. Indeed, Grubraw activity increased mitochondrial transmembrane potential in HeLa cells (Fig. 1g) indicating that the products of Grubraw activity (pyruvate and $FADH_2$) enter mitochondrial oxidative metabolism. D-Ala itself did not affect mitochondrial transmembrane potential.

Moreover, Grubraw activity increased oxygen consumption rate in HeLa cells both under fasting conditions (Fig. 1h) and in rich culture medium (Fig. 1i). We concluded that in HeLa cells, even when substrates in the medium are sufficient, the ETC does not function at the maximal physiological rate, likely due to the regulation of mitochondrial transporters and other metabolic “switching nodes” biased toward aerobic glycolysis. Pyruvate and/or $FADH_2$ produced by

Grubraw can contribute to ETC function independently of these mechanisms and increase the proportion of OXPHOS in cellular metabolism.

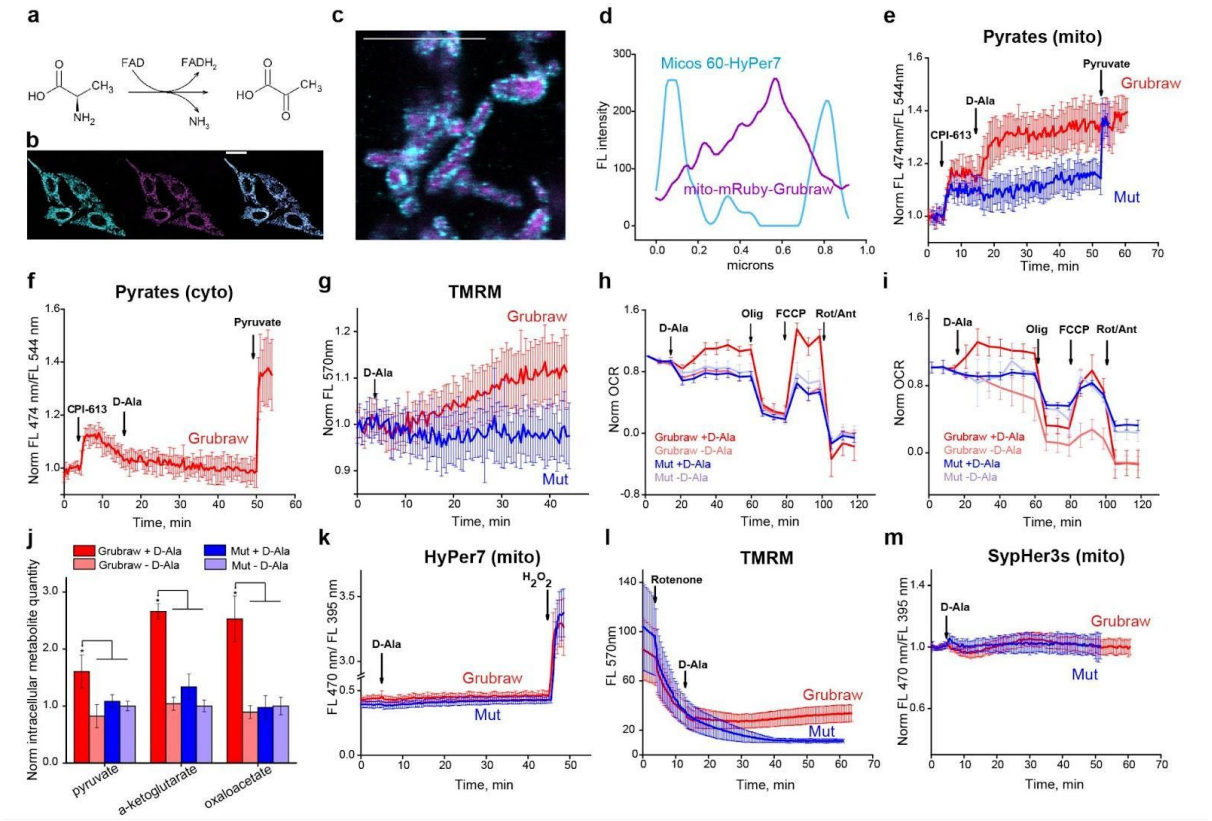


**Figure 1. Grubraw activity in the mitochondria of the Hela Kyoto cells activates OXPHOS. a,** The conversion of D-alanine to pyruvate catalyzed by DadA. **b,** Fluorescence image of HeLa Kyoto cells expressing mito-mRuby-DadA stained with mitoTracker Green. **c,** Fluorescence image of HeLa Kyoto cells expressing mito-mRuby-DadA and Micos60-HyPer7. **d,** A representative fluorescence intensity profile along a cross-section of a mitochondrion from **c**. **e,** Mitochondrial pyruvate concentration in the presence of 120 μM CPI-613 by Pyrates sensor localized in the mitochondria. n = 14 – 15. **f,** Cytosolic pyruvate concentration in the presence of 120 μM CPI-613 by Pyrates sensor localized in the cytosol. n = 6. **g,** Mitochondrial membrane potential by TMRM. n = 12 – 23. **h,** The effect of Grubraw activity on OCR in HBSS medium without glucose. **i,** The effect of Grubraw activity on OCR in DMEM medium with 5 mM glucose. **j,** The effect of Grubraw activity on intracellular TCA cycle metabolites. Mean normalized values ±SD are shown **k,** ROS production by HyPer 7 sensor localized in the mitochondria. n = 8. **l,** Mitochondrial membrane potential by TMRM in presence of 100 μM rotenone. n =21 . **m,** Mitochondrial matrix pH by Sypher3s sensor localized in the mitochondria. n = 18 – 20.
Scale bar represents 25 μm in **b** and 5 μm in **c**.
In **e, f, k, m**, red lines are for HeLa Kyoto cells expressing mRuby-Grubraw and blue lines for the cells expressing mRuby-Grubraw-mut.
In **g, l**, red lines are for HeLa Kyoto cells expressing EGFP-Grubraw and blue lines for the cells expressing EGFP-Grubraw-mut.
In **e, f, g, h, i, k, l, m,** mean or mean normalized values ±SD for n cells are shown for every time point.

What is more, Grubraw activity increased the intracellular concentrations of some TCA cycle metabolites, namely α-ketoglutarate and oxaloacetate, as shown by mass-spectrometry (Fig. 1j). Moreover, intracellular concentration of pyruvate also increased. These results suggest that not only was ETC function affected by Grubraw activity, but general matrix metabolism was also enhanced, likely due to the entrance of Grubraw-derived pyruvate into the TCA cycle.

Thus, the increase in the matrix pyruvate concentration *per se* is able to enhance the TCA cycle flux.

Since we had no direct data about the acceptor of electrons from $FADH_2$ of Grubraw, it was essential to confirm that they are not transferred to $O_2$ thus generating ROS, and that Grubraw activity does not induce oxidative stress in mitochondria. Moreover, the Warburg effect is sometimes thought to be a part of the antioxidant defense system in cancer cells[2,12]. Given these considerations, we used the ultrasensitive genetically encoded $H_2O_2$ probe HyPer7 targeted to the mitochondrial matrix[13]. No changes in HyPer7-mito signal were detected after D-Ala addition in HeLa cells expressing active and inactive Grubraw (Fig. 1k). Thus, Grubraw does not generate physiologically significant $H_2O_2$ concentrations[14], nor does acceleration of OXPHOS elevate endogenous mitochondrial $H_2O_2$ production.

For the DadA homologue from *Esherichia coli*, electron transfer from FAD to $Q_{10}$ analogues with various isoprenoid side chain lengths was demonstrated[15]. Since Grubraw was active in mitochondria and did not generate ROS, and since the purified enzyme was not able to reduce $NAD^+$ or $NADP^+$ *in vitro* (data not shown), we speculated that it could transfer its electrons to some specific acceptor in the ETC, most probably to $Q_{10}$. In presence of the complex I inhibitor rotenone, Grubraw activity prevented complete loss of the mitochondrial transmembrane potential, in contrast to the inactive control enzyme version (Fig. 1l), which suggested that the electrons from Grubraw entered the ETC downstream of the inhibited complex I, likely via the Q-pool, and thus partially maintained mitochondrial function. Additionally, rotenone and all other small-molecule inhibitors used in this work were proven *in vitro* to have no effect on Grubraw enzymatic activity (Extended Data Fig. 1f).

Moreover, the genetically encoded pH sensor SypHer3s [16] with a matrix localization sequence did not report any significant pH changes when Grubraw was active (Fig. 1m). Thus, ammonia released during Grubraw functioning did not affect mitochondrial pH.

Grubraw activity significantly reduced the growth rate of HeLa cells, but D-Ala itself did not affect proliferation. (Extended Data Fig. 1g). These data suggest that oxidative metabolism intensification, at least at the level induced by Grubraw, significantly alters cellular proliferation.

The increase in TCA cycle metabolite pools generated by Grubraw could affect not only the mitochondrial oxidative reactions, but also processes in the cytosol. For example, the increase in oxaloacetate and α-ketoglutarate pools might enhance the function of the malate-aspartate shuttle, which in turn might change the cytosolic $NAD^+$/NADH ratio. Indeed, the genetically encoded fluorescent sensor SoNar[17] demonstrated oxidation of the cytosolic NAD pool during Grubraw activity in HeLa cells (Fig. 2a).

The increase in cytosolic $NAD^+$ concentration might increase the rate of glycolysis, since the $NAD^+$ supply is a limiting factor in this pathway, especially in cells of the Warburg metabolic type. However, the Grubraw activity did not change the rate of intracellular glucose metabolization, as shown by the genetically encoded fluorescent sensor for glucose FLII12Pglu-700μΔ6[18] (Fig. 2b).

The cytosolic $NAD^+$/NADH ratio is coupled to the balance of lactate and pyruvate production by LDH. Thus, we hypothesized that Grubraw-induced cytosolic NADH depletion results in decreased lactate export. However, no significant changes in extracellular lactate concentration were observed in HeLa cells expressing Grubraw after incubation with D-alanine compared to the control cells expressing Grubraw-mut and/or incubated without D-alanine (Fig. 2c).

Therefore, we speculated that the change in cytosolic $NAD^+$/NADH ratio is compensated by enhanced pyruvate export, despite not being conventional for Warburg metabolic cells type. Indeed, Grubraw activity increased extracellular pyruvate concentration in HeLa cell culture (Fig. 2d) both in the presence and absence of glucose in the culture medium. It should be noted

that, in the presence of glucose, some basal level of pyruvate export existed in all samples. Under fasting conditions, no extracellular pyruvate was detected in the samples before D-alanine addition. These data show that HeLa cells strictly regulate OXPHOS rate and matrix pyruvate concentration, exporting the excessive pyruvate into the extracellular medium.

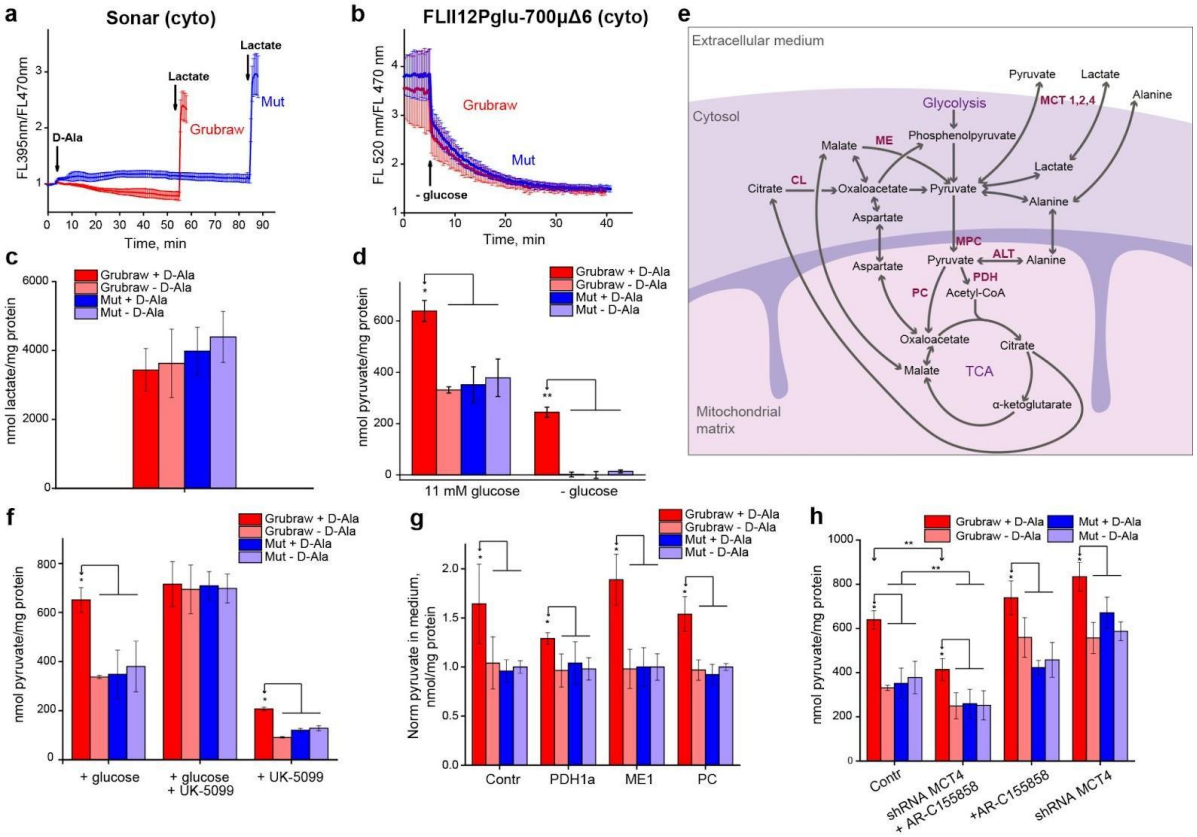


**Figure 2. Grubraw activity increases extracellular pyruvate export in HeLa cells| a,** NAD+/NADH ratio by SoNar sensor. n = 14 – 18 cells. **b,** Glycolysis rate by FLII12Pglu-700μΔ6 glucose sensor. n = 14 cells. **c**, The effect of Grubraw activity on extracellular lactate. **d,** The effect of Grubraw activity on extracellular pyruvate in presence and absence of 11 mM glucose. **e,** Possible biochemical pathways for export of pyruvate from the mitochondrial matrix into the extracellular medium. The key enzymes and transporters are labeled in purple letters, and the metabolites are labeled in black letters. **f,** The effect of Grubraw activity on extracellular pyruvate. MPC activity was inhibited by 10 μM UK-5099 in presence and absence of 11 mM glucose. **g,**.The effect of Grubraw activity on extracellular pyruvate. PDH1a, ME1, and PC were downregulated by RNA interference. The control cells expressed a scrambled shRNA. In all samples, 11 mM glucose was present in the medium. **h,** The effect of Grubraw activity on extracellular pyruvate. MCT 1,2 and/or MCT4 activity was inhibited using 0.5 μM AR-C155858 and RNA interference, respectively. In all samples, 11 mM glucose was present in the medium

In **a** and **b**, red lines are for HeLa Kyoto cells expressing mRuby-Grubraw and blue lines are for cells expressing mRuby-Grubraw-mut. Mean or mean normalized values ±SD for n cells are shown at every time point.

The data in **c, d, f, h** represent mean pyruvate or lactate quantity in the medium normalized to protein quantity in the sample ±SD. In plot **g**, these values were normalized to the corresponding value in the “Grubraw-mut - D-alanine” sample. Mean values ±SD are shown. *p<0.05

We were next interested in the pathway by which pyruvate exits the mitochondrial matrix (Fig. 2e). MPC transports pyruvate molecules together with protons, so it is unlikely to perform reverse pyruvate transport against the proton concentration gradient. Indeed, incubation of the cells in glucose-free medium with the selective MPC inhibitor UK-5099 (10 μM) did not prevent enhanced Grubraw-dependent pyruvate export (Fig. 2f). In the control samples, however, pyruvate concentration also was not zero, probably because the residual cytosolic pyruvate could not be transported into mitochondria and was directed to the extracellular medium instead. It is of note that, UK-5099 did not influence the enzymatic activity of Grubraw *in vitro*

(Extended Data Fig. 2b) nor D-alanine transport (Extended Data Fig. 1h). The latter result indicates that D-alanine transport into the mitochondrial matrix does not depend on MPC. We demonstrated that in presence of glucose, the extracellular pyruvate concentration increased in all control samples compared to the samples without UK-5099, probably because of the increased proportion of glycolysis-derived pyruvate in the export flux (Fig. 2f).

Therefore, we hypothesized that matrix pyruvate is converted into some intermediates which are transported to the cytosol and turned back into pyruvate there. These might be aspartate, malate, citrate, or alanine (Fig. 2e). To clarify which exact mechanism is used, we knocked down key enzymes involved in the possible export pathways, namely pyruvate dehydrogenase (PDH), pyruvate carboxylase (PC), and malic enzyme (ME1), in HeLa Kyoto cells expressing active and inactive versions of Grubraw. The mRNA quantities of PDH1a subunit, PC, and ME1 (cytosolic isoform) were decreased roughly 30-, 4-, and 5-fold, respectively, compared to the control cell line expressing scrambled shRNA (Extended Data Fig. 2a), which resulted in a significant protein quantity decrease, as shown by mass-spectrometry analysis (Extended Data Fig. 2b). Grubraw-dependent pyruvate export was retained in all knockdown cell lines. However, in the cells with PDH1a knockdown the difference was markedly decreased (Fig. 2g). This indicates that pyruvate is oxidized and enters the TCA cycle to be exported from the mitochondrial matrix.

Next, we studied the roles of monocarboxylate transporters (MCTs) in Grubraw-induced pyruvate export. MCTs 1, 2, 3, and 4 perform proton-coupled transport of pyruvate, lactate, and some other monocarboxylic acids through the plasma membrane. However, MCT3 is expressed only in some tissues of the eye[19], so we focused our attention on MCTs 1, 2, and 4. We obtained HeLa Kyoto cell lines with stable active and inactive Grubraw expression and shRNA-mediated MCT4 knockdown (MCT4 mRNA quantity decreased roughly 9-fold, (Extended Data Fig. 2a and b). On the other hand, we inhibited MCT1 and MCT2 activity using the selective inhibitor AR-C155858 (0.5 μM). None of these conditions alone affected pyruvate export. However, when MCT4 knockdown and MCT1 and MCT2 inhibition were performed simultaneously, extracellular pyruvate concentrations proportionally decreased in all samples (Fig. 2h). These data suggest that MCT1, MCT2, and MCT4 are all involved in pyruvate export and are interchangeable.

To better understand how Grubraw-derived pyruvate enters cell metabolism and shifts metabolic fluxes, we performed $^{13}C$ metabolic labeling experiments. HeLa cells expressing Grubraw were cultured for 24 hours in a medium with labeled carbon sources (glucose or glutamine). Focusing on acute effects of Grubraw activation, we changed the growth media to HBSS solution containing labeled carbon substrate (with only labeled glucose, or a mixture of glucose and glutamine with only one labeled component), added D-alanine and incubated cells under these conditions for 90 minutes before extraction (Extended Data Fig. 3d).

In labeled glucose only medium, we used 1,2-$^{13}C$-glucose as it can provide information on glycolysis and the pentose-phosphate pathway[20–22] (Fig. 3a, 3b). Intra- and extracellular pyruvate in this experiment had almost the same isotopologue distribution (Fig. 3c, Extended Data Fig. 3b) with about half of all pyruvate having two labeled carbons. Activation of Grubraw for 90 min led to a significant decrease in the M+2 isotopologue relative to M+0 in both intra- and extracellular pyruvate, intracellular α-KG and OA, and extracellular lactate (Fig. 3c). This “isotopic dilution” occurs because pyruvate from D-alanine evidently has a natural isotopic distribution, confirming the existence of a carbon flux from the Grubraw-derived mitochondrial pyruvate pool to the pyruvate pool in the extracellular medium.

At the same time, the probability of OA M+1 behaves strictly differently (Fig. 3a, 3b). In all control cells, the probability of OA M+1 corresponds to the natural occurrence of the isotope,

while the “Grubraw+D-Ala” sample contained elevated OA M+1 isotoplogue. In contrast, the probability of α-KG M+1 was increased in all labeled samples (Fig. 3d). Only the C1 α-KG carbon is removed during the [α-KG → OA] conversion in the TCA cycle. Thus, isotopologues with an increased content of α-KG M+1 must carry the tracer atom predominantly in the C1 position in order to turn into an OA pool with a negligibly small amount of tracer. However, fragmentation analysis (Extended Data Fig. 3a, 4) showed that only 10% of α-KG M+1 isotopologues were labeled at the C1 position. Therefore, we assume that OA is not synthesized from α-KG in TCA. This may be due to the incomplete TCA turning, which is characteristic of Warburg-type metabolism[22]. On the other hand, Grubraw-derived additional pyruvate influx can activate full turning of the TCA cycle and/or PC activity (Fig. 3b), resulting in an increase in M+1 OA isotopologue probability. Both activated metabolic pathways lead to OXPHOS intensification that correspond to our SeaHorse experiments (Fig. 1h, 1i).

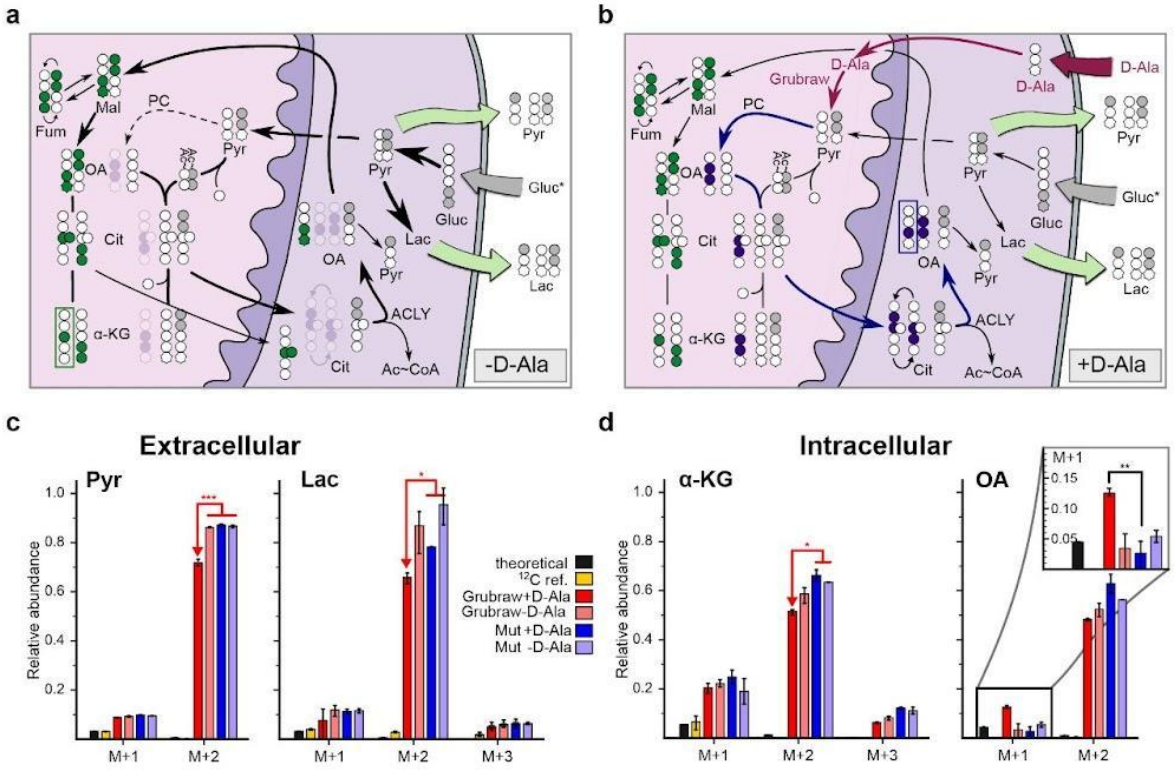


**Figure 3. Major metabolic fluxes in HeLa cells growing on a medium with 1,2-$^{13}C_2$-glucose as the only carbon source. a, b,** Carbon label migration from glucose over the central metabolism in the absence (**a**) and presence (**b**) of Grubraw activity. Labeled carbon atoms are colored gray (●) by default; green (●) when they entered the matrix as the C4 metabolite; and blue (●) when they entered the TCA cycle via PC reaction. **c,** Isotopologue probability distribution for extracellular pyruvate and lactate molecules. **d,** Isotopologue probability distribution for intracellular OA and α-KG molecules. All probabilities are normalized to M+0 one. The derivatizer effect on the distributions was removed. Data on the labeling probability of C1 atoms for this experiment is provided in Extended Data Fig. 3a.

We also conducted an experiment with two carbon sources, glucose and glutamine, considering these conditions to be closer to physiological conditions. Here we performed parallel labeling - the addition of two substrates, in which the first is labeled, and the second is unlabeled, and vice versa. We called these two states Q*G and G*Q for labeling with glutamine and glucose, respectively. Possible label migration through central metabolism from glutamine is shown on Fig. 4a and 4b, isotopomers distributions are shown on panels c – e.

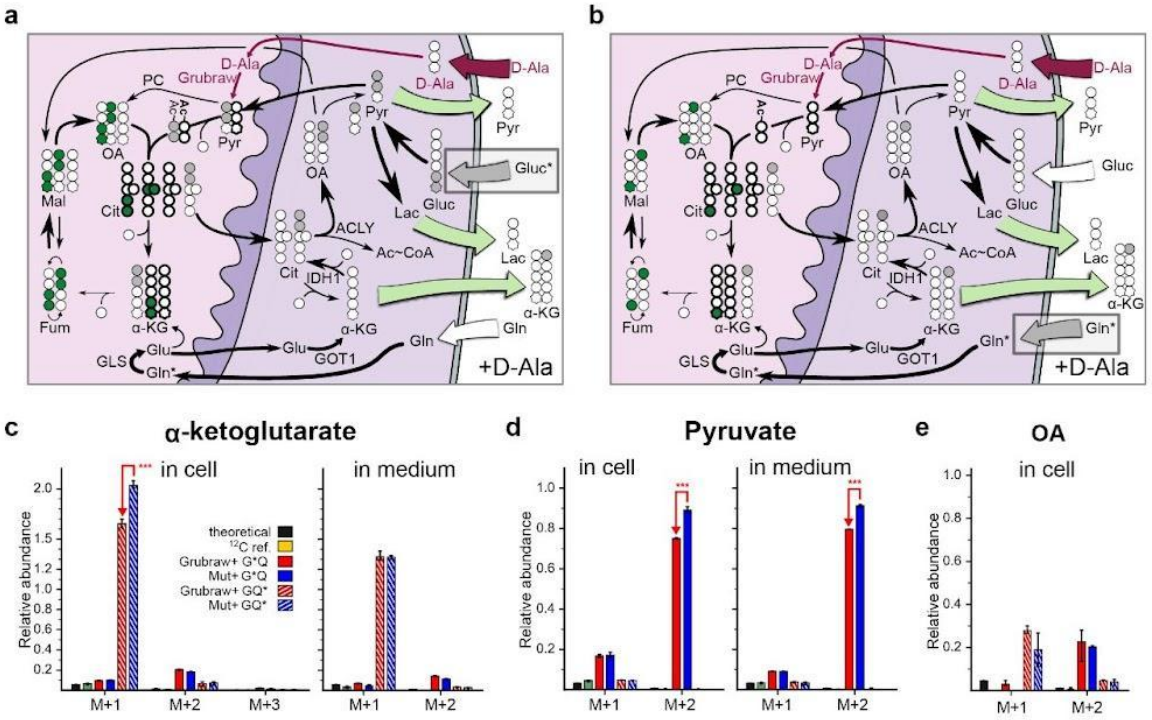


**Figure 4. Major metabolic fluxes in HeLa cells growing on a poor medium with 1,2-$^{13}$C-glucose/glutamine or glucose/5-$^{13}$C-glutamine.**
**a, b,** Carbon label migration from glucose (**a**) and glutamine (**b**) in the presence of Grubraw activity. Labeled carbon atoms are colored gray (●) by default; green (●) when they entered the matrix as the C4 metabolite. **c-e,** Isotopologue probability distribution of α-ketoglutarate (**c**), pyruvate (**d**) and oxaloacetate (**e**) Data for both intra- and extracellular metabolites are shown in (**c, d**). All probabilities are normalized to M+0. The derivatizer effect on the distributions was removed. Data on the labeling probability of the $C_1$ atom for this experiment is provided in Extended Data Figure 3c.

Under these conditions, glucose supplied lower carbon input into the metabolism relative to glutamine: α-$KG_{M+2}$ and $OA_{M+2}$ relative abundance was about 20% in G*Q samples (Fig. 4c,e) versus roughly 60% in G* only samples (Fig. 3d). The influx of unlabeled carbons from D-Ala was detected by the significant dilution of $Pyr_{M+2}$ in G*Q samples and intracellular α-$KG_{M+1}$ in Q*G samples (Fig. 4d and 4c). Interestingly, dilution of α-$KG_{M+1}$ by Grubraw activation in Q*G samples is observed in the intracellular pool, but not in the extracellular pool. One possible explanation is shown on Figure 4a and 4b. Glutamine-derived α-KG may enter the metabolism directly via the TCA cycle and indirectly via reductive carboxylation by IDH1 or IDH2. Glutamine catabolism begins with hydrolysis to glutamate catalyzed by matrix glutaminase. Subsequently, glutamate is deaminated to α-KG by aminotransferases in the cytosol or mitochondrial matrix (GOTx, GDH, AST). We propose that 5-carbon molecules can be transported from the mitochondrial matrix to the cytosol due to the concentration gradient, after which the glutamine tracer enters the metabolism predominantly via cytosolic IDH (IDH1):

$$\cdot KG \rightarrow [IDH1] \rightarrow \textbf{iso-Cit} \rightarrow \textbf{Cit} \rightarrow \textbf{OA} \rightarrow \textbf{Asp} \rightarrow [\text{to matrix}] \\ \rightarrow \textbf{Mal} \rightarrow [\text{to matrix}] \qquad (1)$$

In this case, the α-KG carbon enters the matrix as the C4 metabolite after mixing with glucose-derived C4 metabolite. The cytosolic pool of α-KG does not mix directly with the

mitochondrial pool and appears to be less sensitive to Grubraw-derived carbon influx. This hypothesis is also supported by the strong difference between the occurrence of α-$KG_{M+1}$ and $OA_{M+1}$ in Q*G samples: the abundance of α-$KG_{M+1}$ is 200% relative to the M+0 isotopologue whereas for OA it is just 20%. If α-$KG_{M+1}$ enters the matrix according to (1) under this condition, then 50% of OA becomes unlabelled. Further, OA is mixed in the matrix with OA obtained from glucose, and the probability of it being labeled drops to 16% (Fig. 4e).
In the experiments with the glutamine label, we did not see any tracer atoms in pyruvate. This is not surprising since pyruvate is formed primarily from glucose. The small part that could be derived from α-KG via pathway (2) is also mostly unlabeled because of the tracer position in glutamine (Fig. 4a, 4b).
Finally, this analysis gives an idea about how pyruvate is exported from the matrix. The appearance of additional intramatrix pyruvate increases the OA pool. As a result, the amount of citrate and α-KG is also increased. Additional citrate is exported more actively and leads to an increased level of OA in the cytosol; this additional OA may be partly converted into pyruvate via nonspecific decarboxylation, PEPCK-dependent decarboxylation, or through malate by cytosolic malic enzyme (ME1). Since ME1 knockdown did not affect the pyruvate export flux induced by Grubraw, the former pathways seem to be more probable.

We next tested whether the excessive mitochondrial pyruvate export was an effect characteristic of HeLa Kyoto cells only, or if it was typical for different cancer cell lines of the glycolytic metabolic type. We obtained cancer cell lines HT29 (human colorectal cancer), MDA-MB 231 (human triple-negative breast adenocarcinoma), WM164 and Lu451 (human melanoma), and non-cancer line H9C2 (immortalized rat cardiomyoblasts) stably expressing active and inactive Grubraw (Extended Data Fig. 5a – d). Under the same experimental conditions as HeLa cells, all cancer cell lines demonstrated Grubraw-dependent pyruvate export (Fig. 5a). On the contrary, in the H9C2 cell line the Grubraw-induced pyruvate export was far less pronounced. In melanoma cell lines, lactate export was proven to be independent of Grubraw activity (Fig. 5b). Moreover, Grubraw activity in melanoma cell lines led to an increase in OCR (Fig. 5c, 5d).

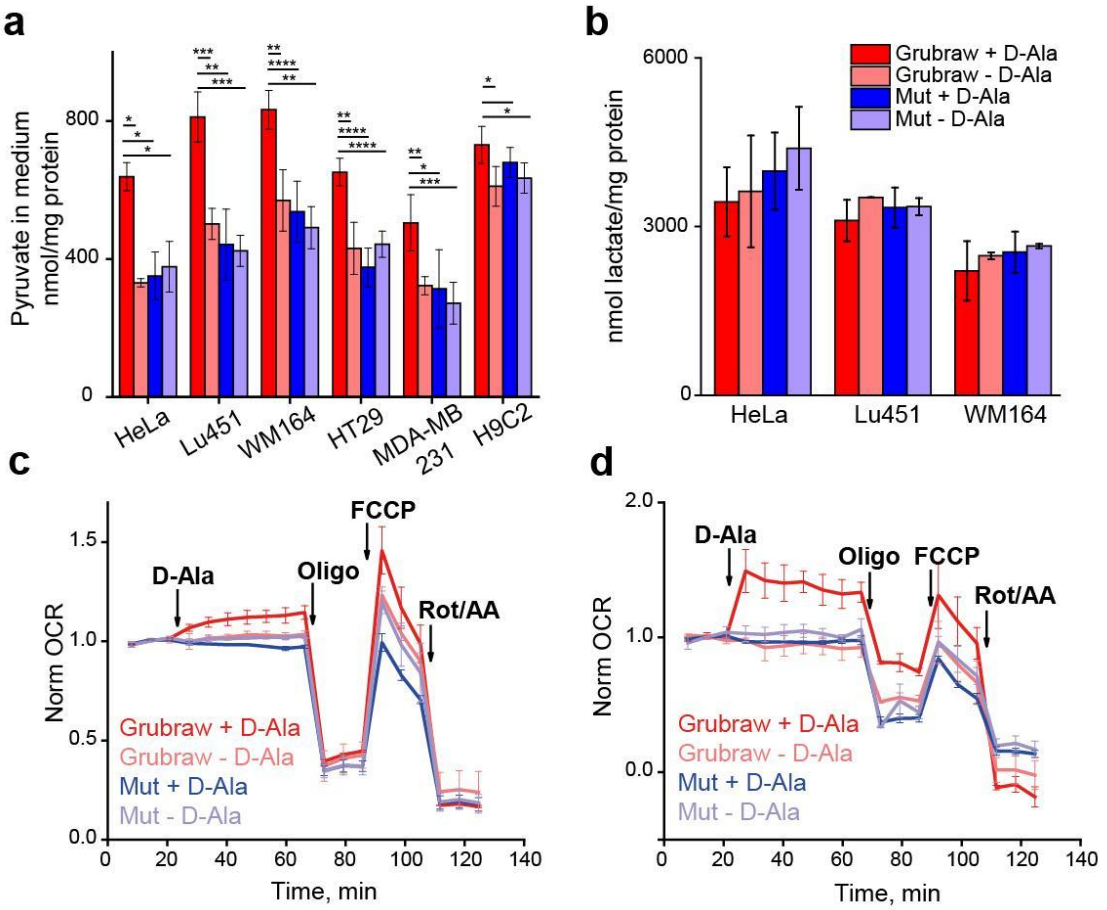


**Figure 5. Grubraw activity modulates metabolism in different cancer cell lines. a,** The effect of Grubraw activity on extracellular pyruvate in a panel of cancer cell cultures. For reference, the data for HeLa Kyoto cells from Fig. 2a are present. **b,** The effect of Grubraw activity on extracellular lactate in melanoma cultures. For reference, the data for HeLa Kyoto cells from Fig. 2c are present. **c,** The effect of Grubraw activity on OCR in WM164 cells. **d,** The effect of Grubraw activity on OCR in Lu451 cells.
Data in **a** and b represent mean pyruvate or lactate quantity in the medium normalized to protein quantity in the sample ±SD. *p<0.05, **p<0.005,***p<0.0005, ****p<0.00005
In **c** and **d**, mean OCR normalized to the corresponding OCR in the zero time point ±SD is shown at every time point for 2-3 biological replicates for every sample.

Summarizing the data presented above, we have identified pyruvate release by cells as a specific mechanism associated with control of the level of pyruvate (or, more generally, control of the carbon flux) in the mitochondrial matrix of cells with Warburg-type metabolism. In oxidative metabolic type cells, like H9C2[23], this mechanism functions much more weakly. We believe that this is a previously undescribed mechanism that allows cancer cells to control the activity of mitochondria in addition to the commonly accepted restriction of pyruvate intake to the matrix.
We next tested whether Grubraw activity affected tumor growth rate in the Lu451 xenograft model in immunodeficient Nude mice. Lu451 cells with stable firefly luciferase and active or mutant Grubraw expression were obtained using CRISPR genome editing (Extended Data Fig. 6a). Luciferase activity and Grubraw-dependent pyruvate export were proven in cell culture (Extended Data Fig. 6b, 6c). An *in vitro* proliferation test with or without D-Ala revealed a difference in cell division rate between Lu451-Fluc-P2A-Grubraw and the inactive mutant (Fig. 6a).

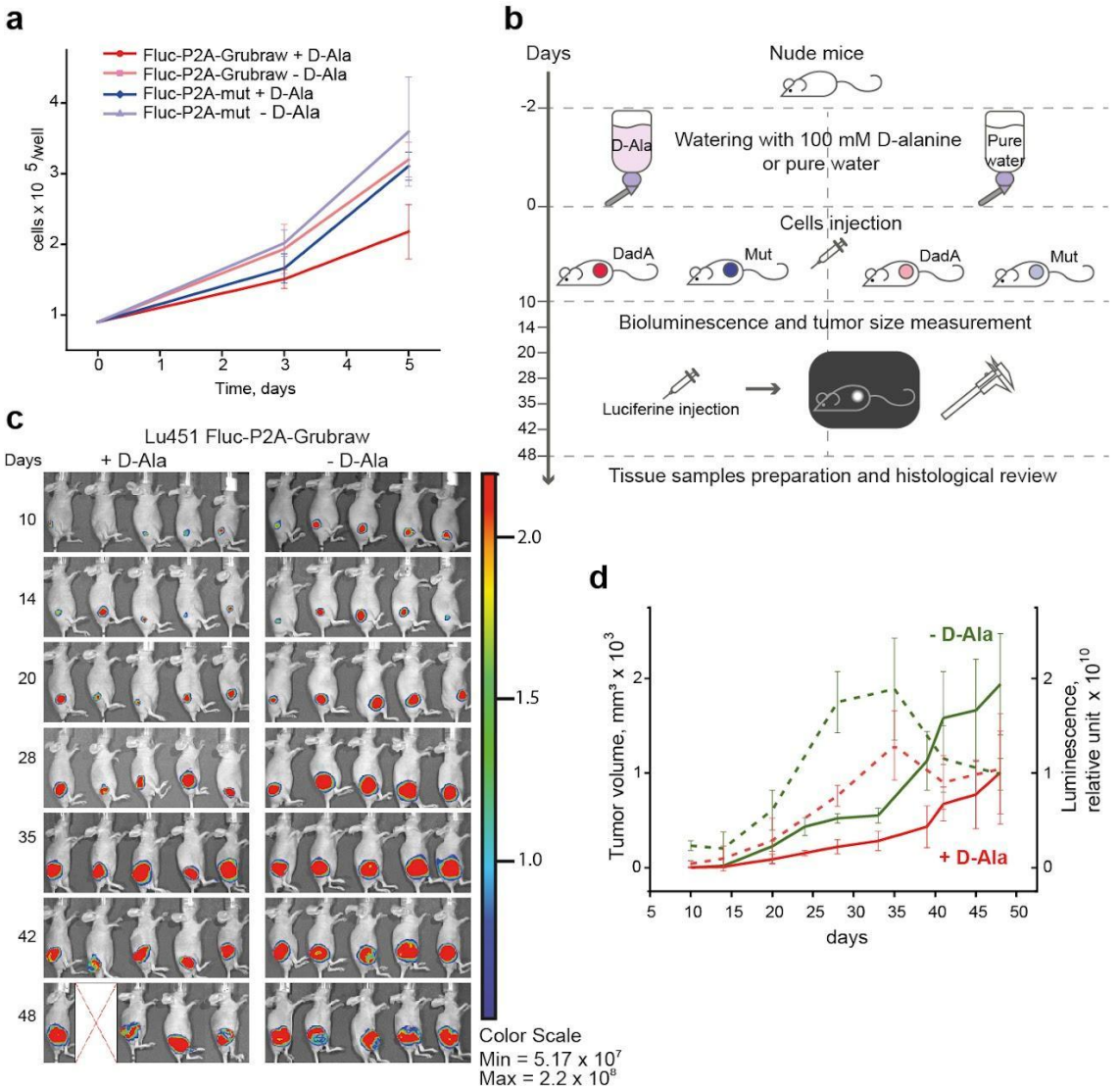


**Figure 6. Grubraw activity slows down tumor growth *in vivo*. a,** The effect of mRuby-Grubraw activity on Lu451 cell culture growth. **b,** The design for the experiment with the Lu451 xenograft model. **c,** Bioluminescence in tumors expressing luciferase and mRuby-Gubraw throughout the experiment. **d,** The effect of Grubraw activity on tumor volume (solid lines) and bioluminescence (dashed lines). Mean values ±SD are shown.

The scheme of the experiment with mice is shown in Fig 6b. Depending on the group, mice with subcutaneously grafted cells received either 0.1M D-Ala in drinking water, or just pure water. In the control group with xenografts expressing mutant Grubraw, D-alanine did not affect tumor growth rate (Extended Data Fig. 6d). In the groups with xenografts expressing active Grubraw, D-Ala decreased tumor growth rate, especially 14 – 28 days after tumor cells injection. By day 28 the mean tumor volume in the group watered with D-Ala was about 2-fold smaller than in the group watered with pure water (Fig. 6c, 6d). Tumor necrotization started 28 days after injection in the water drinking group and after 35 days in the group watered with D-Ala (Fig. 6d). Histological review of tissue sections 48 days after xenograft implantation did not reveal any microscopic changes in the lungs, liver, brain, nor lymph nodes of the experimental animals (Extended Data Fig. 6 e – h). On day 48, the size of necrosis reached up to 50% of the tumor size in the water group, and up to 30% in the D-alanine group (Extended Data Fig. 6l). After necrosis had started, the luminescence began to decrease in all groups, and the dispersion in

tumor size inside the groups increased. No toxic effects of 0.1 M D-alanine, including significant weight loss (Extended Data Fig. 5j), were observed in these mice. Our results show that activated mitochondrial metabolism markedly slows down melanoma growth *in vivo*.

In summary, we created a chemogenetic tool named **Grubraw** capable of activating mitochondrial metabolism in cancer cells. Mitochondrial activation with Grubraw involves the production of pyruvate and $FADH_2$ by enzymatic oxidation of D-Ala in the matrix, increasing oxygen uptake following TCA cycle and ETC activation. Grubraw can be used to activate mitochondria of cells with low mitochondrial pyruvate intake as a result of a genetic mutation or a decrease in expression level, which is characteristic of various cancer cells[24–26]. Apparently, the activity of Grubraw associated with the transfer of electrons from $FADH_2$ to quinones can partially compensate for disturbances in the operation of the electron transport chain associated with mutations or other pathological disorders of complex I. We observed that the mitochondrial pyruvate produced by Grubraw is partially secreted into the extracellular medium by cancer cells, while in cardiomyoblasts with a more pronounced oxidative type of metabolism this effect was very weak. We found that reversing the Warburg effect by activating mitochondrial metabolism leads to a decrease in tumor growth rate. Our data suggest that the Warburg effect, at least in some cancer cell lines, is realized by regulating a limited list of key points in metabolism, such as mitochondrial pyruvate transport. In this case, mitochondrial metabolism is reversibly limited due to the restriction in oxidation substrates rather than totally inhibited due to mutations in housekeeping genes. This mechanism provides metabolic flexibility for cancer cells so that they can effectively survive changes in nutritional conditions, metabolism-targeted therapy, and other challenges. A deep understanding of the mechanisms underlying the metabolic heterogeneity of cancer cells, combined with multiple metabolic nodes targeted for treatment, gives hope for a cure for cancer in the future.

**Grubraw, a chemogenetic generator of mitochondrial pyruvate, reveals new mechanisms of mitochondrial metabolic control that underlay the Warburg effect**

# REFERENCES


1. Warburg, O. (1956). On the Origin of Cancer Cells. Science *123*, 309–314. 10.1126/science.123.3191.309.
2. Vaupel, P., and Multhoff, G. (2021). Revisiting the Warburg effect: historical dogma versus current understanding. J Physiol *599*, 1745–1757. 10.1113/JP278810.
3. Bensard, C.L., Wisidagama, D.R., Olson, K.A., Berg, J.A., Krah, N.M., Schell, J.C., Nowinski, S.M., Fogarty, S., Bott, A.J., Wei, P., et al. (2020). Regulation of Tumor Initiation by the Mitochondrial Pyruvate Carrier. Cell Metabolism *31*, 284-300.e7. 10.1016/j.cmet.2019.11.002.
4. Schell, J.C., Olson, K.A., Jiang, L., Hawkins, A.J., Van Vranken, J.G., Xie, J., Egnatchik, R.A., Earl, E.G., DeBerardinis, R.J., and Rutter, J. (2014). A role for the mitochondrial pyruvate carrier as a repressor of the Warburg effect and colon cancer cell growth. Mol Cell *56*, 400–413. 10.1016/j.molcel.2014.09.026.
5. Lee, M.S., Moon, E.J., Lee, S.W., Kim, M.S., Kim, K.W., and Kim, Y.J. (2001). Angiogenic activity of pyruvic acid in in vivo and in vitro angiogenesis models. Cancer Res *61*, 3290–3293.
6. Cevatemre, B., Ulukaya, E., Dere, E., Dilege, S., and Acilan, C. (2021). Pyruvate Dehydrogenase Contributes to Drug Resistance of Lung Cancer Cells Through Epithelial Mesenchymal Transition. Front Cell Dev Biol *9*, 738916. 10.3389/fcell.2021.738916.
7. Huasheng, L., Forbes, R.A., and Verma, A. (2002). Hypoxia-inducible factor 1 activation by aerobic glycolysis implicates the Warburg effect in carcinogenesis. J Biol Chem *277*, 23111–23115. 10.1074/jbc.M202487200.
8. He, W., Li, C., and Lu, C. (2011). Regulation and Characterization of the dadRAX Locus for D -Amino Acid Catabolism in Pseudomonas aeruginosa PAO1 . Journal of Bacteriology *193*, 2107–2115. 10.1128/JB.00036-11.
9. Hamase, K., Morikawa, A., Etoh, S., Tojo, Y., Miyoshi, Y., and Zaitsu, K. (2009). Analysis of small amounts of D-amino acids and the study of their physiological functions in mammals. Anal Sci *25*, 961–968. 10.2116/analsci.25.961.
10. Kiriyama, Y., and Nochi, H. (2016). D-Amino Acids in the Nervous and Endocrine Systems. Scientifica *2016*. 10.1155/2016/6494621.
11. Bulusu, V., Prior, N., Snaebjornsson, M.T., Schultz, C., Sauer, U., Aulehla, A., Bulusu, V., Prior, N., Snaebjornsson, M.T., Kuehne, A., et al. (2017). Spatiotemporal Analysis of a Glycolytic Activity Gradient Linked to Mouse Embryo Mesoderm Article Spatiotemporal Analysis of a Glycolytic Activity Gradient Linked to Mouse Embryo Mesoderm Development. Developmental Cell *40*, 331-341.e4. 10.1016/j.devcel.2017.01.015.
12. Zheng, J. (2012). Energy metabolism of cancer: Glycolysis versus oxidative phosphorylation (review). Oncology Letters *4*, 1151–1157. 10.3892/ol.2012.928.
13. Pak, V.V., Ezeriņa, D., Lyublinskaya, O.G., Pedre, B., Tyurin-Kuzmin, P.A., Mishina, N.M., Thauvin, M., Young, D., Wahni, K., Martínez Gache, S.A., et al. (2020). Ultrasensitive Genetically Encoded Indicator for Hydrogen Peroxide Identifies Roles for the Oxidant in Cell Migration and Mitochondrial Function. Cell Metab *31*, 642-653.e6. 10.1016/j.cmet.2020.02.003.
14. Sies, H. (2014). Role of metabolic H2O2 generation: redox signaling and oxidative stress. J Biol Chem *289*, 8735–8741. 10.1074/jbc.R113.544635.
15. Olsiewski, P.J., Kaczorowski, G.J., and Walsha, C. (1980). Purification and properties of D-amino acid dehydrogenase, an inducible membrane-bound iron-sulfur flavoenzyme from Escherichia coli B *. The Journal of Biological Chemistry *255*.
16. Ermakova, Y.G., Pak, V.V., Bogdanova, Y.A., Kotlobay, A.A., Yampolsky, I.V., Shokhina, A.G., Panova, A.S., Marygin, R.A., Staroverov, D.B., Bilan, D.S., et al. (2018). SypHer3s: a genetically encoded fluorescent ratiometric probe with enhanced brightness and an improved dynamic range. Chem Commun (Camb) *54*, 2898–2901. 10.1039/c7cc08740c.

17. Zhao, Y., Hu, Q., Cheng, F., Su, N., Wang, A., Zou, Y., Hu, H., Chen, X., Zhou, H.-M., Huang, X., et al. (2015). SoNar, a Highly Responsive NAD+/NADH Sensor, Allows High-Throughput Metabolic Screening of Anti-tumor Agents. 777–789. 10.1016/j.cmet.2015.04.009.
18. Takanaga, H., Chaudhuri, B., and Frommer, W.B. (2008). GLUT1 and GLUT9 as the major contributors to glucose influx in HEPG2 cells identified by a high sensitivity intramolecular FRET glucose sensor. Biochim Biophys Acta *1778*, 1091–1099. 10.1016/j.bbamem.2007.11.015.
19. Halestrap, A.P., and Meredith, D. (2004). The SLC16 gene family—from monocarboxylate transporters (MCTs) to aromatic amino acid transporters and beyond. Pflugers Arch - Eur J Physiol *447*, 619–628. 10.1007/s00424-003-1067-2.
20. Antoniewicz, M.R. (2015). Methods and advances in metabolic flux analysis: a mini-review. Journal of Industrial Microbiology and Biotechnology *42*, 317–325. 10.1007/s10295-015-1585-x.
21. Antoniewicz, M.R. (2018). A guide to 13C metabolic flux analysis for the cancer biologist. Exp Mol Med *50*, 1–13. 10.1038/s12276-018-0060-y.
22. Vaitheesvaran, B., Xu, J., Yee, J., Lu, Q.-Y., Go, V.L., Xiao, G.G., and Lee, W.-N. (2015). The Warburg effect: a balance of flux analysis. Metabolomics *11*, 787–796. 10.1007/s11306-014-0760-9.
23. Romero, N., Swain, P., and Dranka, B. Characterization of Glycolysis with a Panel of Common Cellular Models Using Agilent Seahorse XF Technology.
24. Chai, Y., Wang, C., Liu, W., Fan, Y., and Zhang, Y. (2019). MPC1 deletion is associated with poor prognosis and temozolomide resistance in glioblastoma. J Neurooncol *144*, 293–301. 10.1007/s11060-019-03226-8.
25. Li, X., Ji, Y., Han, G., Li, X., Fan, Z., Li, Y., Zhong, Y., Cao, J., Zhao, J., Zhang, M., et al. (2016). MPC1 and MPC2 expressions are associated with favorable clinical outcomes in prostate cancer. BMC Cancer *16*, 894. 10.1186/s12885-016-2941-6.
26. Xue, C., Li, G., Bao, Z., Zhou, Z., and Li, L. (2021). Mitochondrial pyruvate carrier 1: a novel prognostic biomarker that predicts favourable patient survival in cancer. Cancer Cell Int *21*, 288. 10.1186/s12935-021-01996-8.
27. Crooks, G.E., Hon, G., Chandonia, J.-M., and Brenner, S.E. (2004). WebLogo: A Sequence Logo Generator. Genome Res. *14*, 1188–1190. 10.1101/gr.849004.
28. Lamprecht, W., Heinz, F., and Bergmeyer, H.U. (ed. ) (1988). Pyruvate. In Methods of Enzymatic Analysis (VCH Publishers (UK) Ltd.), pp. 570–577.
29. Livak, K.J., and Schmittgen, T.D. (2001). Analysis of relative gene expression data using real-time quantitative PCR and the 2(-Delta Delta C(T)) Method. Methods *25*, 402–408. 10.1006/meth.2001.1262.
30. Zimmermann, M., Sauer, U., and Zamboni, N. (2014). Quantification and Mass Isotopomer Profiling of α-Keto Acids in Central Carbon Metabolism. Anal. Chem. *86*, 3232–3237. 10.1021/ac500472c.
31. Long, C.P., and Antoniewicz, M.R. (2019). High-resolution 13C metabolic flux analysis. Nat Protoc *14*, 2856–2877. 10.1038/s41596-019-0204-0.

**Acknowledgements**

This paper is dedicated to the memory of Vladimir Skulachev and Andrey Vinogradov, two great Russian scientists who contributed enormously to the field of mitochondrial research. We want to acknowledge Lubov I. Golubeva and Ekaterina S. Kovaleva from Joint-Stock Company “Ajinomoto Genetika Research Institute” for advice in planning and interpreting mass isotopomer measurements.

**Author Contributions**

E.S.P. and D.Y.B. designed the research; carried out biochemical, cell and microscopic experiments; designed molecular cloning; analyzed data from imaging, in vitro and in vivo experiments and co-wrote the paper. A.V.I. carried out CRISPR technologies. A.A.M. carried out lentivirus production. D.A.K., A.E.K. designed and carried out proteomics, mass spectrometry and metabolomics analyses. A.M.N. designed and performed bioinformatic analyses and co-wrote the paper. N.F.Z. and A.V.I. carried out oxygen consumption rate measurement. L.E.S. and M.V.S. performed experiments with mice. O.V.L. carried out extracellular lactate measurement. O.I.P. performed immunohistochemistry and histological review of mouse tissues. I.B. helped with melanoma culturing. V.V.B. directed the research and co-wrote the paper.

**Author Information**

Correspondence and requests for materials should be addressed to E.S.P. (potekh2975@gmail.com), or V.V.B. (belousov@fccps.ru).

# Methods

**Gene cloning and mutagenesis**

We synthesized cDNA of the *Pseudomonas aeruginosa* DadA gene (GenBank: AUB04911.1) at Evrogen (https://evrogen.com/). The DadA was cloned into the pQE30 vector using BamHI/SacI restriction sites (see primer list). The cDNA of DadA was fused with mRuby or EGFP via a Gly-Ser-Gly linker containing the BamHI restriction site and subcloned into the pQE30 vector using the BglII/SacI sites in the primers and BamHI/SacI in the vector.

For expression in the eukaryotic cell mitochondrial matrix, cDNAs of the FP-fused DadA were subcloned into the second generation lentiviral vector pLCMV-Puro with an N-terminal tandem dimer of COX8 presequences using BamHI site in the vector and BglII in the flanking primers.

Primers with nucleotide substitutions leading to Tyr17Ala and Tyr18Ala in the predicted FAD binding domain of the DadA were generated. The mutated DadA gene fragment lacking 18 end base pairs was amplified using dadA-Y17A/Y18A-Fw and DadA-SacI-Rv primers. Then the missing base pairs were added using dadA-BamHI-long-Fw primer which overlapped with the 5`-end of dadA-Y17A/Y18A-Fw primer.

Primer sequences are presented in Supplementary in Table 1.

All genetic construct sequences were verified by Sanger sequencing.

**Multiple Sequence Alignment**

The amino acid sequence of DadA from *Pseudomonas aeruginosa* (GenBank: AUB04911.1) was aligned in BLAST against the SwissProt database. 9 sequences of 60 – 70% similarity were selected, and multiple global alignment in Clustal W was performed using default parameters. For visualization, a logo was created using WebLogo 3 [27].

**Protein purification**

DadA variants were expressed in *E. coli* strain XL1 Blue using pQE30 plasmid with the His6 tag on the N-end of target protein. Bacterial Protein Extraction Reagent (Thermo Scientific) was used for bacteria lysis. Centrifuged lysate was purified by gravity-flow chromatography on TALON Metal Affinity Resin (Clontech) following the manufacturer's protocol with 0.05% Triton X-100 added to all buffers. Fractions containing target protein were desalted and concentrated on Amicon Ultra 10K centrifugal filter units (Merck Millipore), and the final protein preparation was stored in PBS containing 0.05% Triton X-100 at 4°C.

**SDS-PAGE**

The purity and concentration of DadA preparations were evaluated using SDS-PAGE in 12% separating gel with Coomassie staining. Protein concentration was evaluated using BSA standards (100 – 1000 ng/lane) loaded in the same gel. The standard curve was plotted in ImageJ.

**DadA activity assay**

DadA activity was measured in microplates as described in [8] with minor alterations. The reaction mix contained 100 mM Tris-HCl (pH 8.0), 0.8 mM phenazine methosulfate, 0.8 mM nitroblue tetrazolium, 20 mM D-Ala, 0.2 mM FAD (optionally) and 0.5 – 1 µg protein. All DadA preparations demonstrated the same activity with and without additional FAD. The $D_{620}$ increase was registered at 37°C. A Varioscan Lux (Thermo Scientific) plate spectrophotometer was used in this and all following plate assays. To prove that metabolic inhibitors do not affect DadA

activity, 100 μM rotenone,120 μM CPI-613, 10 μM UK-5099, or 0.5 μM AR-C155858 was added to the reaction mix. All activities were normalized to wild type DadA activity without inhibitors.
To test whether DadA could reduce $NAD^+$ or $NADP^+$, the reaction mix containing 100 mM Tris-HCl (pH 8.0), 2 or 10 mM $NAD^+$ or $NADP^+$, 20 mM D-Ala, and 0.5 – 1 ug protein was used. The $D_{340}$ increase was registered at 37°C.
All measurements were performed in 2 – 3 technical replicates.

**Pyruvate assay**
The cell cultures with stable mRuby-Grubraw or mRuby-Grubraw-mut expression were incubated in HBSS with 20 mM HEPES and 11 mM glucose (except as noted). To inhibit MPC or MCT 1 and 2, 10 μM UK-5099 or 0.5 μM AR-C155858, respectively, were added to the medium. After 40 min incubation at 37°C and 5% $CO_2$, 10 mM D-alanine was added, and the cells were incubated for 1 h 15 min. Pyruvate concentration in the centrifuged extracellular medium samples (5 min 18000 g, 4°C) was measured in microplates using Pyruvate Assay kit (Abcam) or as described in [28].
The cells were lysed in RIPA buffer, centrifuged (5 min 18000 g, 4°C), and protein concentration in the supernatant was measured using the BCA Protein Assay kit (Sigma).
Total pyruvate content in the well normalized to total protein content (5 – 7 biological replicates) was compared by t-test with Holm adjustment. For knockdown HeLa samples, these values were additionally normalized to the corresponding control value (Grubraw-mut without D-alanine) and compared using the Kruskal-Wallis rank sum test and Dunn test with Holm adjustment.

**Lactate assay**
The samples were collected as described in pyruvate assay protocol. Lactate concentration was measured using Lactate Assay kit II (Sigma) or Radiometer ABL800 FLEX device. Total lactate content in the well was normalized to total protein content as described in the pyruvate assay protocol. 2 biological replicates were analyzed.

**Cell culturing**
HeLa Kyoto cells (gender: F) were cultured in RPMI 1640 (Sigma) containing 10% FBS v/v (Biosera), 2 mM L-glutamine (Paneco), 100 U/mL penicillin (Paneco) and 100 mg/mL streptomycin (Paneco) at 37 °C in a 5% CO2 atmosphere.
Lu451 (gender: M) and WM164 (gender: M) cells were maintained in DMEM medium (Paneco) containing 4.5 g/L glucose and 5% FBS, 2 mM L-glutamine (Paneco), 100 U/mL penicillin (Paneco) and 100 mg/mL streptomycin (Paneco) at 37 °C in a 5% CO2 atmosphere.
HT29 (gender: F), MDA-MB 231 (gender: F), HEK 293 TN (gender: F), H9C2 cells were cultivated in DMEM medium (Paneco) containing 4.5 g/L glucose and 10% v/v FBS, 2 mM L-glutamine (Paneco), 100 U/mL penicillin (Paneco) and 100 mg/mL streptomycin (Paneco) at 37 °C in a 5% CO2 atmosphere.

**shRNA Cloning:**
shRNA plasmids to knockdown PDH1a, ME1, PC and MCT4 expression by RNA interference were created based on pGreenPuro lentivector (System Biosciences, LLC). The shRNA template was made by annealing appropriate oligonucleotides to each other (Extended Data Fig. 3) and then cloned into the unique BamHI or EcoRI sites in the vector.

**Generating cell lines with stable protein or shRNA expression**

The HeLa Kyoto, HT29, MDA-MB 231, and H9C2 cell lines stably expressing Grubraw variants or shRNAs were generated by lentiviral transduction followed by cell sorting.
Lu451 and WM164 cell lines stably expressing Grubraw variants were generated by CRISPR genome editing followed by cell sorting.

**Lentivirus production**
HEK 293 TN cells were seeded at 5 × 104 cells/cm$^2$ in 25 cm$^2$ tissue culture flasks. After 22 hours, cells were transfected using linear 40 KDa polyethyleneimine (Polysciences) at a mass ratio of 1:3 (DNA:PEI), with the respective plasmids: 5 µg of vector genome; 2.5 µg pMDLg/pRRE; 2.5 µg of pRSV-REV; 2.5 µg of VSV-G envelope. Medium was replaced 18-22 hours after transfection. After another 48-hour period, the supernatant was harvested, clarified at 0.45 µm and stored at −80 °C. The resulting virus concentration was about 2*10^6 TU/ml.

**Lentiviral transduction**
The cells were seeded on culture plastic so that they were transduced at 60% confluency. Polybrene was added to a concentration of 8 µg/ml. After 2 – 3 days, the transduced cells began to fluoresce and were collected by cell sorting.

**Cell sorting**
Cells suspended in ice-cold HBSS with 20 mM HEPES and 11 mM glucose were sorted on a Sony MA9000 Sorter and collected into 0.5 ml of cultivation medium. mRuby fluorescence was excited by a 561 nm laser, EGFP or GFP fluorescence was excited by a 488 nm laser. For cells expressing both fluorescent proteins (green and red), manual fluorescence spillover compensation was used.

**CRISPR genome editing**
The intron of the PPP1R12C gene at the AAVS1 locus of chromosome 19 was chosen as the insertion site. A bicistronic lentiCRISPRv2-Blast (https://www.addgene.org/83480/) plasmid carrying SpCas9 was used, into which the guide RNA sequence was cloned under the U6 promoter at the BsmBI restriction sites. Double strand DNA for gRNA cloning was made by annealing oligonucleotides gRNAgRNA-AAVS1-2-dir and gRNA-AAVS1-2rev to each other (Suppl. Table 1).
A donor plasmid carrying the insertable construct between the homology arms was created based on the AAV-CAGGS-EGFP plasmid (https://www.addgene.org/22212/). EGFP was replaced by MCS containing homologous arms obtained by annealing the oligonucleotides Ins-dir-NcoI and Ins-rev-MluI to each other (Supp. Tabl.1). Overlap extension PCR was used for connection of firefly luciferase with mRuby-Grubraw or mRuby-Grubraw-mut by P2A self-cleaving peptide, and then PCR-products were introduced into the MCS region digested with AgeI and KpnI using GeneArt™ Gibson Assembly HiFi Master Mix according to manufacturer protocol.
Two-component transfection with the Grubraw donor plasmid and SpCas9/gRNA plasmid was used to transiently express SpCas9 and gRNA followed by editing the melanoma Lu451 cell genome. Five days after transfection, cells were selected for knock-in with 1.5 µg/ml puromycin. After selection, cells were validated for mRuby signal using FACS (Fluorescent-Activated Cell Sorting) (Sony MA900).

**qPCR**

RNA was extracted from cultured cells using the ExtractRNA kit (Evrogen) according to the manufacturer's protocol. OneTube RT-PCR SYBR kit (Evrogen) was used for cDNA production by reverse transcription followed by qPCR. Primers for the human housekeeping gene TUBA1B, and the PDH1a, ME1, PC, and MCT4 genes are described in Extended Data Fig. 3. Relative changes in genes expression were analyzed with the $2^{-\Delta\Delta Ct}$ method[29].

**Transfection**

For HeLa Kyoto cells, FuGENE HD Transfection Reagent (Promega) was used. The cells were seeded on plastic or confocal dishes 2 days before the experiment and transfected 1 day before the experiment.

**Microscopy**

Fluorescent imaging was performed using an Eclipse Ti2-E microscope (Nikon), the NIS-Elements program (Nikon) and a monochrome Prime BSI digital camera (Teledyne Photometrics), if not otherwise stated. Image analysis and editing was performed in ImageJ and Nikon Analysis programs. The digital data were analyzed and plotted in Origin 2015. For imaging parameters, see Supplementary Table 2.

To confirm the mitochondrial localization of DadA, cells expressing active or inactive mRuby-Grubraw and EGFP-Grubraw were stained with MitoTracker Green (ThermoFisher Scientific) or20 nM TMRM, respectively. Mitochondrial membrane potential was also evaluated by TMRM fluorescence.

To confirm the matrix localization of DadA, HeLa Kyoto cells coexpressing mRuby-Grubraw and HyPer7-Micos60 were imaged on a Nikon Ti2 confocal microscope with a Nikon A1 LFOV monochrome digital camera.

$H_2O_2$ generation was evaluated using HyPer7 [13] with a mitochondrial matrix localization signal. In this and all further time-lapse experiments, HeLa Kyoto cells expressing mRuby-Grubraw or mRuby-Grubraw-mut were used. At the end of the imaging session, 100 μM $H_2O_2$ was added to prove sensor functioning.

Matrix pH dynamic was evaluated using SypHer3s [16] with a matrix localization sequence.

$NAD^+$/NADH ratio dynamics was registered using SoNar [17]. At the end of the imaging session, 2.5 mM sodium lactate was added as a positive control to prove sensor functioning.

Pyruvate concentration dynamics in the cells was evaluated using Pyrates [11]. To model physiological glycolysis flux and cytosolic pyruvate concentration, 11 mM glucose was added to the imaging medium. To inhibit PDH, 120 μM CPI-613 was added. To activate DadA, 10 mM D-alanine was added. At the end of the imaging session, 30 mM pyruvate was added to prove sensor functioning.

Glucose concentration dynamics in the cells was evaluated using FLII$^{12}$Pglu-700μδ6 [18]. The cells were seeded into μ-slides (iBiDi). The culture medium was replaced with imaging medium with 10 mM D-alanine and 11 mM D-Glucose 30 min before the experiment. After the baseline sensor signal was registered, the medium was replaced by imaging medium with 10 mM D-alanine. Imaging parameters were the same as for the Pyrates sensor.

In all experiments, the cells were incubated in imaging medium (HBSS medium with 20 mM HEPES) for 30 min at 37°C and 5% $CO_2$, then the baseline sensor signal was registered for ~5 min, after which 10 mM D-alanine was added (if not otherwise stated). Sensor fluorescence ratio or TMRM fluorescence intensity in every cell was normalized to the corresponding mean value for the baseline in this cell. These normalized values were averaged for n cells. For

HyPer7 and FLII12Pglu-700μδ6, the non-normalized sensor fluorescence ratio was averaged for n cells. All experiments were performed in 2 – 3 replicates.
Murine tumor and tissue sections were imaged in brightfield mode with a Nikon DS-Fi3 Color Camera and 20x objective.

**Oxygen consumption rate measurement**

OCR was measured using Seahorse Mito Stress Test on Seahorse XF Analyzer (Agilent) according to the manufacturer's protocol with minor alterations. Cells expressing mRuby-Grubraw or mRuby-Grubraw-mut were incubated in HBSS or cultivation medium without $HCO_3^-$ for 30 min at 37°C without $CO_2$. Basal OCR was registered for 18 min. Then 10 mM D-alanine or HBSS was added and OCR was registered for 42 min. Subsequently1 μM oligomycin, 1 μM FCCP, and 1 μM antimycin + 1 μM rotenone were added, with 18 min OCR measurement after every administration. OCR data for each well were normalized to basal OCR. Data for 3-5 biological replicates (wells) were averaged.

**LC-MS and LC-MS/MS analysis of ketoacids**

Samples were derivatized with phenylhydrazine (PH) using a procedure adapted from [30]. The derivatizing reagent (DR) was a freshly prepared 2 mM solution of PH base in acetonitrile-methanol-water mixture (2:2:1 v/v). For intracellular samples the cultural medium was removed and cells were incubated with 1 ml of DR (1h, -20°C). For extracellular samples an aliquot of cultural medium was mixed with DR (1:9) and incubated (1h, -20°C). Then the liquid phases were centrifuged and dried under vacuum (25°C) and dissolved in solvent A. The column in the HPLC system was a Thermo C18 Hypersil Gold 100×2.1mm, 1.9 μm. SolventA consisted of 5% acetonitrile, 0.3% triethylammonium formate (TEA) in water, and solvent B consisted of 0.3% TEA in acetonitrile. The following gradient was used: 0-3 min: isocratic 5%B, 23 min: 45%B, 24-29 min: isocratic 90% B. The mass-spectrometer (Thermo Q-Exactive HF, HESI-II ion source) was operated in negative ion mode. To register MS1 for PH derivatives we used single ion monitoring mode with 60 000 resolution at three m/z ranges: 176.066-180.066 (Pyr); 220.100-224.100 (OA); 234.100-238.100 (α-KG). MS2 spectra of these substances were registered in separate runs of parallel reaction monitoring mode for precursor ions: 177.066, 178.070, 179.073, 221.056, 222.060, 223.063, 235.072, 236.075, 237.0786, 238.0795 m/z at 30,000 resolution and HCD energy 10 (Extended Data Fig. 4b). For absolute quantitation of extracellular pyruvate and α-KG, we prepared a series of pure substance dilutions in a fresh cultural medium. MIDs were extracted from MS1 runs and corrected to natural isotope occurrence utilizing MS2 data. Additionally, we extracted the probabilities of tracer inclusion into the first position in a molecule from MS2 data . Details on spectra processing, the equation for MID correction, and statistical inference are provided in the Supplementary Methods.

**GC-MS analysis**

The cell medium was treated with cold methanol (4:1), refrigerated (1 hour, -22°C) and centrifuged (14000 g, 10 min). 1.5 ml of each supernatant were transferred to a new microcentrifuge tube and derivatized with MSTFA as described in [31]. D-Norvaline was added before the procedure as an internal standard for concentration measurements. The GC–MS system was a Shimadzu TQ8040 GC–MS, with an Agilent CP-Sil 8 CB (50m × 0.25 mm i.d. × 0.25 μm) column. The carrier gas was UHP-grade helium at 0.88 mL/min. GC–MS analysis of the prepared samples was performed as described in [31]. 0.5 μL was injected in the split mode at a ratio of 1:50 with two or three replicates. For control of the GC–MS system, data collection and initial preprocessing, the Shimadzu GCMS Postrun Analysis software was used. Mass

isotopomer distributions (MIDs) for lactate were extracted from raw spectra (Extended Data Fig. 4d) using self-made scripts. Procedures and tools used for identification, peak integration and MID transformations are described in the Supplementary Methods.

**Targeted proteomics**

Cells were treated with cold 80% methanol (30 min), scraped and centrifuged (10000 g, 5 min). The pellet was washed with cold acetone, resuspended in 100 mM $(NH_4)HCO_3$ (pH 8.0, 0.2% w/v Promega ProteaseMax) and sequentially treated with TCEP (5 mM, 1h, 50ºC), iodoacetamide (15 mM, 1h, RT) and Trypsin Gold (1 µg, 3h, 37ºC). Then, formic acid was added (up to 1% v/v), the samples were centrifuged (10000 g, 5 min), supernatants transferred to new tubes and vacuum-dried. Aliquots were taken from supernatants for peptide measurement and also dried. Dried samples were dissolved in the solution (2% acetonitrile, 0.05% TFA). The mass-spectrometer was a Thermo Q-Exactive HF-X. The HPLC system was a Thermo UltiMate 3000. The chromatography conditions used were the following Column - Thermo Acclaim PepMap RSLC 0.075×150 mm; Solvent A - 0.1% formic acid in water; Solvent B - 80% acetonitrile and 0.1% formic acid in water; Gradient - 4%-45% B in 90 min, 90-100 min - isocratic 95% B; Flow - 300 nanoliters/min. For mass spectra registration the data dependent mode was used and the MS1 range was 350-1500 *m/z*, the number of precursors was 20, and the MS2 range was 200-2000 *m/z*. Separate runs of the samples were performed under the same chromatographic conditions in single ion monitoring mode of several peptides originating from the proteins of interest. Raw data were processed using the standard proteomics protocol and then the peaks of most abundant peptides were quantified separately using self-made scripts (the details are described in the Supplementary Methods).

**Proliferation test**

Hela Kyoto cell lines were seeded on cell culture dishes at a density of 8000 cells/cm$^2$, and Lu451 lines at a density of 10000 cells/cm$^2$. The concentration of D-glucose in the growth medium was 1 g/l. The number of cells in the wells was counted using Luna Cell Counter (ThermoFisher Scientific) with Trypan blue staining. 3 biological replicates were analyzed.

**Murine xenograft model**

The experiments were carried out on 20 female, 6-week-old, athymic nude mice, purchased from the SPF animal facility of the Institute of Biology and Biomedicine of Lobachevsky State University of Nizhny Novgorod (Russia). All animal experiments were approved by the Ethics Committee of the Privolzhsky Research Medical University (Nizhny Novgorod, Russia), approval #6 from April 17, 2019.

Lu451 cells with CRISPR/Cas9 generated stable firefly luciferase and mRuby-Grubraw or mRuby-Grubraw-mut expression were used. $1.5*10^6$ cells in serum-free DMEM were injected subcutaneously into Nude mice. 2 groups of mice with mRuby-Grubraw or mRuby-Grubraw-mut expressing xenografts were watered with 0.1 M D-Ala from 2 days before the injection untill the end of the experiment (48 days after the injection), while 2 identical groups receivedpure water as control. Every group consisted of 4 – 5 animals. The mice were anesthetized with 2% isoflurane before tumor measurement. Xenograft tumor diameter was measured every 4—7 days with a caliper. Tumor bioluminescence was imaged using an IVIS Spectrum imaging system (Caliper Life Sciences, Hopkinton, MA, USA) every week from day 10 after cell implantation. Luciferin solution (150 mg/kg) was administered intraperitoneally 10 minutes before the visualization. The images were analyzed using Living Image software. After the end of the experiment, the mice were weighed, euthanized by an overdose of isoflurane, and the

tumors, brains, lungs, and livers were isolated and fixed in buffered formaldehyde and delivered to histopathological expertise.

**Luciferase assay in cells**

HBSS with 0.3 mg/ml luciferine was added to Lu451 cells with stable firefly luciferase and mRuby-Grubraw or mRuby-Grubraw-mut expression in a 96-well plate and confluence Bioluminescence kinetics was registered for 5 min.

**Immunohistochemistry of mouse tissue sections**

The organs removed during necropsy (tumor with lymph nodes, liver, lung, brain) were placed in a buffered neutral 10% formalin solution for fixation for 24 hours. After standard histological processing based on isopropyl alcohol (10% buffered formalin - 2 hours, isopropyl alcohol - 18 hours, liquid paraffin - 3 hours), tissue fragments were placed into paraffin blocks. Histological sections with a thickness of 3-4 μm were made using rotary microtomes (CUT4062, SLEE medical, Germany), stained with hematoxylin and eosin according to the standard procedure (dewaxing: ortho-xylene, isopropyl alcohol, staining: Mayer hematoxylin - 8 minutes, watery eosin - 3 minutes, rinsing with running water, dehydration stage: isopropyl alcohol, ortho-xylene) and were enclosed under a cover film (Tissue-Tek Prisma histostainer, Tissue-Tek PrismaFilm, Sacura, Japan).